PHYSICAL REVIEW RESEARCH **1**, 033149 (2019)

Chirality-assisted three-dimensional acoustic Floquet lattices

Yu-Gui Peng,[1,2,*] Ying Li,[2,*] Ya-Xi Shen,[1,*] Zhi-Guo Geng,[1] Jie Zhu,[3,†] Cheng-Wei Qiu,[2,†] and Xue-Feng Zhu[1,†]
[1]*School of Physics and Innovation Institute, Huazhong University of Science and Technology,*
Wuhan, 430074, People's Republic of China
[2]*Department of Electrical and Computer Engineering, National University of Singapore, Kent Ridge 117583, Republic of Singapore*
[3]*Department of Mechanical Engineering, the Hong Kong Polytechnic University, Hung Hom,*
Kowloon, Hong Kong SAR, People's Republic of China

(Received 20 May 2019; published 4 December 2019)

Artificial topological insulators in classical systems are thriving, especially the meta-atom-based three-dimensional (3D) topological lattices. Here we propose a paradigm based on engineering coupling networks in a generalized spatial Floquet lattice, which gives rise to low-loss and broadband 3D topological systems. A mapping between time and space dimensions is utilized to construct the Floquet system with chirality-assisted coupling patterns periodically modulated in spatial dimensions. The cyclotron orbiting motion of sound in the bulk and reversely orbiting motion on the surface are demonstrated, which provides a direct acoustic analogue of the electronic transport in Chern insulators. Weyl points and Fermi arc-like surface states unveil the topological transport of edge states. Splicing together two Floquet lattices with opposite chirality, we realize low-loss topological negative refraction on the surface, where the mirror reflection at the interface is prohibited. Our findings provide diverse ways to construct 3D devices with topological functionalities in acoustics and beyond.

DOI: 10.1103/PhysRevResearch.1.033149

I. INTRODUCTION

The unidirectional and robust control of energy flow in classical wave systems is not reachable before the pioneering works of demonstrating the quantum-Hall-like one-way edge states in photonic crystals [1–3]. Since then, tremendous attention has been drawn to the field of classical analogues of electronic topological insulators in photonics, phononics, and mechanics systems. Recently, various schemes for realizing topological acoustic transport were proposed to construct pesudospin/valley degrees of freedom in two-dimensional (2D) static systems, which are passive and not time-varying, to mimicking the quantum spin/valley Hall effects [4–21]. However, these reported pesudospin/valley-based acoustic topological insulators are still not strictly robust in one-way topological transport, since the bosonic-like time-reversal symmetry in the linear and static acoustic system does not allow any Kramers doublet [22]. An elegant solution is to break the time-reversal symmetry, for example, by introducing angular momentum bias with circulating airflow or active liquid [23–28]. These systems strongly suppress the pesudospin/valley backscattering induced by irregular impurities and support one-way robust chiral edge states on the boundary. However, the precise control of the synchronous rotation frequency and stability of the circulating airflow array is quite challenging, which greatly hinders the practical implementation and the wide range of applications.

In the past years, investigations on topological transport in 3D lattices are rising, mostly based on the delicate tuning of band structures of the meta-atom-based 3D phoxonic crystals [6–8,29–32]. In this paper, we choose a different strategy and propose a unique type of 3D acoustic topological lattice, i.e., acoustic Floquet insulator, where a mapping relation is established between the time dimension and the space dimension. The topological phase transition is triggered simply by varying the coupling strengths in the Floquet framework. 3D topological transport based on the spiral waveguide array was proposed by Rechtsman *et al.* [33]. However, to the best knowledge, there hitherto exists no acoustic counterpart, since the tremendous impedance mismatch between acoustic waveguides and background air will largely suppress the freedom to control the coupling patterns between chiral waveguides (e.g., the helical waveguides). Here, we propose a judicious approach to attach the screwed coupling arms to straight waveguides for creating a generalized Floquet system. By controlling the evolution process of in-plane coupling patterns along the orthogonal dimension, we demonstrate broadband and low-loss chiral modes either in the bulk or on the surface of the 3D Floquet lattices with reversely cyclotron orbiting motions. The topological edge states are verified by the existence of paired Weyl points and Fermi arc-like surface states, as predicted by the calculated band structures. In Floquet systems, since band structure is periodical and unbounded, the Chern number does not necessarily equal to the number of edge states in band gaps. Therefore, we introduce another topological invariant of winding number to describe the number of spinless chiral modes in band gaps

---

[*] These authors contributed equally to this paper.

[†] Authors to whom correspondence should be addressed: jiezhu@polyu.edu.hk; eleqc@nus.edu.sg; xfzhu@hust.edu.cn

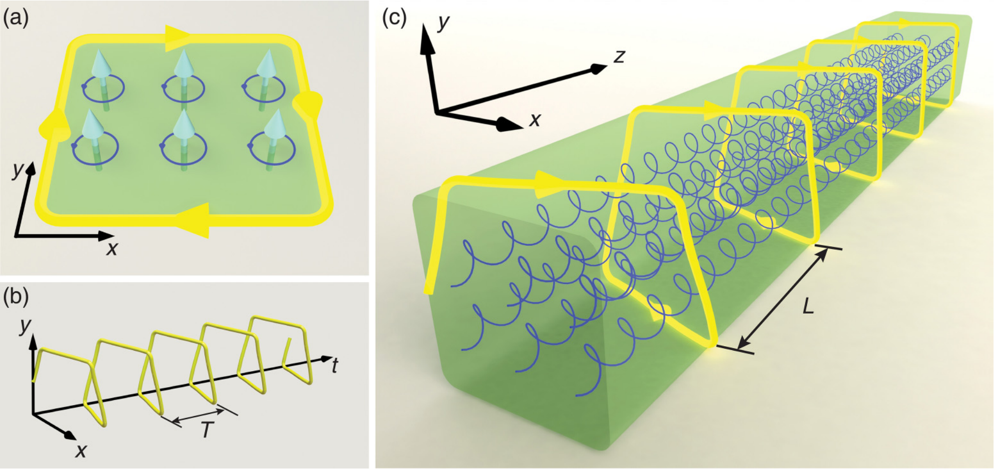

FIG. 1. Mapping between the Chern insulator and 3D Floquet lattice. (a) An illustration of the Chern insulator in an upward magnetic field that supports clockwise propagating electrons on the boundaries, with interior electrons in the anticlockwise cyclotron motion. (b) The propagation of edge states in the Chern insulator. (c) The propagation of edge states in the 3D Floquet lattice. There exists a direct mapping between the time dimension t and the space dimension z.

[34–36]. Splicing together two Floquet lattices of opposite structural chirality, we demonstrate broadband and low-loss topological negative refraction on the crystal surface, for which the mirror reflection at the interface is prohibited and the negative refraction is robust against surface defects. The time-space dimension mapping offers us a new perspective to investigate wave dynamics in time-modulation systems on a static platform, which is practically realizable and controllable. The Floquet acoustic systems, bearing the advantages of low loss, broad operation band, small fingerprint and simple design, pave the way for realizing versatile 3D devices with topological functionalities.

II. RESULTS AND DISCUSSION

Figure 1(a) shows a schematic of the electronic transport in Chern insulators, where electrons subject to magnetic fields follow circular cyclotron orbits. In the bulk, the closed orbits of electrons make the interior insulating. However, the trajectories of electrons at the edges are not locally closed but along the full extent of edges in a chiral way [37]. These strange states are termed as chiral edge states. In Fig. 1(b), we plot the trajectories of electrons in the framework of space time, which is a helical curve under the time evolution. In this work, we reveal that the 3D acoustic Floquet lattice with screwed coupling arms, as shown in Fig. 1(c), can also support chiral edge states in a similar way, providing a direct acoustic version of Chern insulators. Comparing Fig. 1(b) with Fig. 1(c), the trajectories of edge states are both helical with an insightful mapping relation between the time dimension t and the space dimension z. A schematic of the 3D acoustic Floquet lattice is shown in Fig. 2(a), which is composed by 6×6 unit cells in x-y plane and eight spatial modulation periods along the z direction. We can divide one complete period of the spatially modulated coupling process into four steps. In each step, the coupling strength between neighboring waveguides is time-independent and precisely controlled by the couplers. The primitive unit cell of the Floquet lattice is depicted in the inset of Fig. 2(a). It consists of four corner-site waveguides **A** (blue), and one center-site waveguide **B** (red), which is reflected on the x-y plane. In each unit cell, there are one waveguide **A** and one waveguide **B** on average. Along the z axis, the unit cell has four parts, where the couplers (yellow) are arranged between adjacent waveguides to control the coupling pattern. The flexibility in tailoring the coupling shows advantages in exploring rich physics with other interesting coupling patterns, by noting that the coupling strength is only determined by the configuration of couplers. Figure 2(b) shows that the coupling arm is rotated clockwise and modulated along the z direction. By stacking the unit cells along the x, y, z directions, we will obtain 3D acoustic Floquet lattices (Supplemental Material Note 1, Figs. S1 and S2 [38]). The property of coupling arms is presented in Fig. 2(c). Here, we define the coupling strength C by $C = \arcsin(P_{\text{out}}/P_{\text{in}})$, where P_{in} and P_{out} indicate the input and output acoustic pressures through the coupler [26,39]. The dispersion curve shows that sound transmission approaches unitary at around 9.6 kHz with the coupling strength up to 0.5π. In a broad range from 6.0 to 10.1 kHz, the coupling strength remains strong and is larger than 0.38π. At the frequencies under 5.0 kHz or over 11.0 kHz, the coupling is weak ($<0.25\pi$). Figure 2(d) shows the assembled sample for experiments. The sample has eight sections [Fig. 2(e)], where each section is constructed by stacking waveguide layers **L1–L8** [Fig. 2(f)], Supplemental Material Note 1, and Figs. S3, S4 [38]). In the following, we show that topological phase transition will occur in the 3D Floquet lattice, triggered by increasing the coupling strength above the threshold of 0.25π.

In condensed matter physics, the Hamiltonian of Floquet lattices is time dependent. The solution of the time-dependent Schrödinger equation $i\frac{d\psi}{dt} = H(t)\psi$ takes the form of $\psi(t) = U(t)\psi(t_0)$, where $U(t)$ is a unitary time evolution operator [40]. $U(t)$ can be expressed into $U(t) = \mathcal{T}\exp[-i\int_{t_0}^{t} H(t)dt]$, with $\mathcal{T}$ the ordering operator. The stationary states of time-dependent systems are given by the eigenvalues of the time evolution operator as $U(t)\psi(t_0) = e^{i\varepsilon T}\psi(t_0)$, with ε the

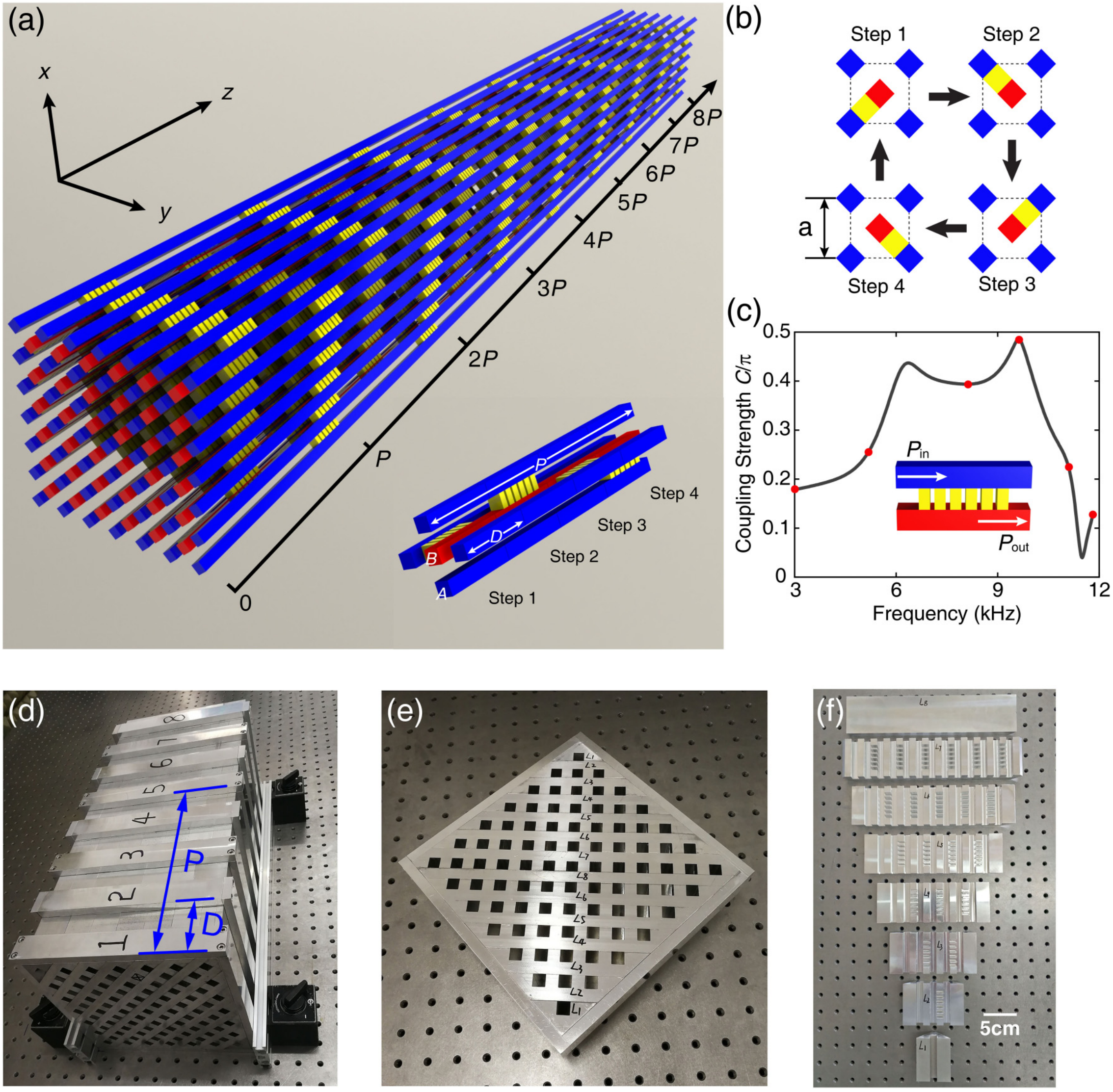

FIG. 2. (a) A schematic of the 3D Floquet lattice, comprising 6 × 6 unit cells in the x-y plane and eight modulation periods along the z direction. The inset shows the unit cell structure with four site waveguides (**A**) on the corner and one coupling waveguide (**B**) in the center. Each unit cell is divided into four parts (Steps 1–4). (b) Coupling patterns in the four steps with the coupling arm rotating in a clockwise loop for a complete modulation period. (c) Coupling strength of the grating structure connecting the site waveguide and the coupling waveguide. (d)–(f) Photographs of the fabricated sample: the assembly with eight sections, one section comprising multiple layers and the layers L1–L8.

defined quasienergy and T the modulation period. In our case, considering the tight-binding approximation, we derive the Bloch Hamiltonian for 3D Floquet lattices [34,35]

$$H(z) = \sum_{m=1}^{4} H_m$$
$$= -\sum_{m=1}^{4} C(z)[\cos(\vec{b}_m \cdot \vec{k})\sigma_x + \sin(\vec{b}_m \cdot \vec{k})\,\sigma_y], \tag{1}$$

where σ_x, σ_y are the Pauli matrices and $\vec{b}_m$ are given by $\vec{b}_1 = (-a/2, -a/2)$, $\vec{b}_2 = (-a/2, a/2)$, $\vec{b}_3 = (a/2, a/2)$, $\vec{b}_4 = (a/2, -a/2)$, with a the spacing between the adjacent site waveguides **A** in Fig. 2(b). The coupling pattern $C(z)$ is periodical along the z. By replacing the time dimension t in the solution of the Schrödinger equation with the space dimension z, we will obtain the evolution operator of the designed Floquet system

$$U(z) = \mathcal{T}\exp\left[-i\int_{z_0}^{z} H(z)dz\right] = e^{-iH_4D}e^{-iH_3D}e^{-iH_2D}e^{-iH_1D}, \tag{2}$$

where H_m represents the Bloch Hamiltonian in the m step in a unit cell and D the quarter of modulation period P. It is worth mentioning that the ordering operator $\mathcal{T}$ makes the step Hamiltonians noncommutative. Therefore, sound will propagate through the four configurations step by step along the $+z$ direction, which makes the mapping of z dimension to pseudotime feasible. Moreover, the flexibility in tailoring coupling arms offers us a possibility to forbid the backward propagation in the z dimension with adiabatic coupling

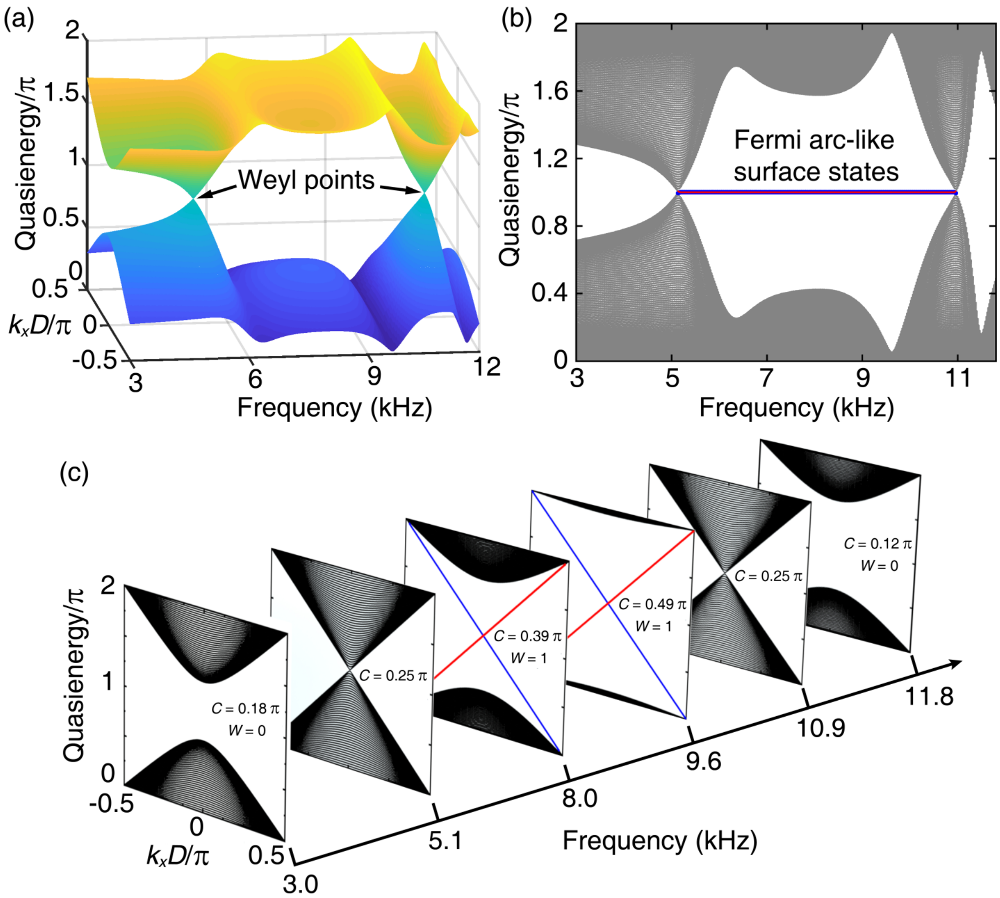

FIG. 3. (a) Quasienergy spectrum where a pair of Weyl points locate at $(k_x,\ k_y,\ f) = (0,\ 0,\ 5.1)$ and $(k_x,\ k_y,\ f) = (0,\ 0,\ 10.9)$, respectively. (b) Acoustic Fermi arc-like surface states denoted by the red and blue lines that connect the Weyl points and correspond to the topological edge states at the leftward and rightward surfaces with opposite group velocities. (c) The projected band structures of acoustic Floquet lattices at different frequencies. The winding number W is nonvanishing, when the coupling strength is above 0.25π.

processes [41]. Eigenspectra of the Bloch Hamiltonian $H(z+P) = H(z+4D) = H(z)$ are solved from the equation $U|\psi(z+4D)\rangle = e^{-i\varepsilon}\ |\psi(z)\rangle$, where U is the coupling-strength-dependent evolution operator, ε is the quasienergy ranging from 0 to 2π in one modulation period (Supplemental Material Note 2, Fig. S5 [38]). By solving the governing equation with the dispersive coupling strength in Fig. 2(c), we obtain a pair of Weyl points locating at $(k_x, k_y,\ f) = (0,\ 0,\ 5.1)$ and $(0,\ 0,\ 10.9)$ in Fig. 3(a), respectively. At the Weyl points, the coupling strength $C = 0.25\pi$. By choosing a supercell strip with the Bloch boundary condition in x direction and the rigid boundary condition in y direction, we further calculate the projected quasienergy band structures (Supplemental Material Note 3 [38]). In Fig. 3(b), we observe the Fermi arc-like surface states at $k_x = 0$, which connect projections of the paired Weyl points, as denoted by the red and blue lines. The Fermi arc-like surface states are actually the topological edge states at leftward and rightward boundaries with positive and negative group velocities, respectively. Here the sign of group velocity is related to the direction of acoustic energy flow. For acoustic waves input in the x-y plane and travelling along the $+z$, positive group velocity is pointed to $+x$ direction on the leftward boundary. The topological phase transition triggered by tailoring the coupling strength is observed in Fig. 3(c). When the coupling is weak, e.g., $C = 0.18\pi$ at 3.0 kHz or $C = 0.12\pi$ at 11.8 kHz, the bulk bands are topologically trivial with zero winding number. As a result, there exist no edge states in the band gap. An exceptional case occurs at 5.1 kHz and 10.9 kHz, where the coupling strength equals to 0.25π in Fig. 3(a). These are the phase transition points or Weyl points at which the band gap is just closed. As the coupling strength surpasses 0.25π, e.g., $C = 0.38\pi$ at 8.0 kHz or $C = 0.49\pi$ at 9.6 kHz, the bulk bands are topologically nontrivial with non-vanishing winding numbers (Supplemental Material Note 4 [38]). A pair of gapless edge state bands are across the band gap, although the Chern number is zero in this static system. Here the edge states in the red and blue bands are spinless, which correspond to the chiral states propagating along the leftward and rightward surfaces of the 3D Floquet lattice with opposite group velocities. The chiral sound transport at the surfaces of 3D Floquet lattices bears a resemblance to the quantum Hall effect after transforming the static 3D system into a 2D time-varying system, i.e., mapping the spatial dimension z to the time dimension t. Therefore, there exists artificial electric fields generated by the chirally modulated coupling patterns, with the direction of artificial electric fields determined by the rotation senses of modulation [33]. When the artificial electric field is reversed, the handedness of topological edge transport is accordingly mirrored.

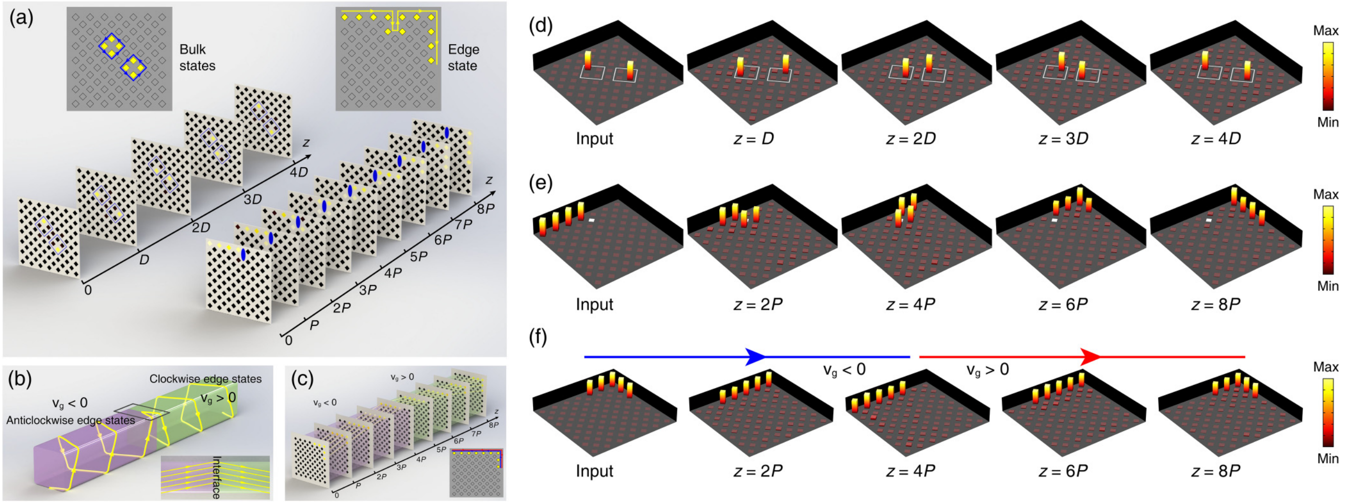

FIG. 4. (a) The simulated sound energy distributions at different planes (x-y plane) along the $+z$, showcasing the cyclotron motion of bulk states and robust unidirectional propagation of edge states. (b) The schematic of topological negative refraction at the interface of two oppositely chirality-assisted 3D Floquet lattices. (c) The simulated sound energy distributions at different planes along the z direction, showcasing topological negative refraction. The blue and red arrows indicate edge states with negative and positive group velocities. (d)–(f) The measured sound energy distributions at different planes along the z direction, showcasing the cyclotron motion of bulk states, the robust unidirectional propagation of edge states, and the topological negative refraction. Here the measured field distributions are normalized by the maximum in each plane and the operating frequency is 9.6 kHz.

We first numerically demonstrate the cyclotron orbiting motion of sound both in the bulk and on the surfaces of the 3D Floquet lattice. Simulation details are appended in Supplemental Material Note 5 [38]. The acoustic energy distributions on different cross-sections (x-y plane) along the z direction are calculated for the coupling strength $C = 0.49\pi$ at 9.6 kHz in Fig. 4(a). From the transverse field evolutions at $z = 0, D, 2D, 3D, 4D$ and $z = 0, P, 2P, 3P, 4P, 5P, 6P, 7P,$ and $8P$, we find that acoustic waves, input at two interior waveguides and four edge waveguides, propagate in chiral senses of anticlockwise and clockwise, respectively. A rigid defect is introduced on the upper boundary, marked by the ellipse that replaces one waveguide. The edge transport is topologically protected as acoustic waves can detour the defect smoothly with near unitary transmission (>96%). If the Floquet lattice is elongated along the z direction, we will observe an acoustic beam advancing helically on the surface with suppressed diffraction. From 6.0 to 10.1 kHz, where the coupling strength is less than unitary but above the threshold, the 3D Floquet lattice still supports topological chiral transport immune against local defects, while the coupling-induced diffraction will lead to surface beam expansion. The chirally modulated coupling patterns generate artificial electric fields that determine the chiral sense of unidirectional transport. Intuitively, for two connected Floquet lattices of opposite chirality, abruptly reversed artificial electric fields at the interface will give rise to the effect of negative refraction, as schematically depicted in Fig. 4(b). The calculated energy distributions in Fig. 4(c) verify our prediction, where topological negative refraction occurs at $z = 4P$. Figures 4(d)–4(f) show the measured sound energy distributions normalized by the maximum at different x-y planes along the z direction, for demonstrating the cyclotron motion of bulk states, robust unidirectional propagation of edge states, and topological negative refraction, which agrees well with simulations. The experimental measurement processes are appended in Supplemental Material Note 5 and Figs. S6, S7 [38]. It is worth noting that the diffraction loss measured in experiments is trivial due to the unidirectional $\boldsymbol{k}$ vector in refraction, since the gapless edge state bands are linear [Fig. 3(c)]. It differs from the topological negative refraction between adjacent surfaces in the Weyl sonic crystals where multiple $\boldsymbol{k}$ vectors in refraction will lead to observable attenuation [8]. We also explore the effect of different boundary conditions on the topological transport in chirality-assisted 3D Floquet lattices, see Supplemental Material Note 6, Fig. S8 [38]. Different from the active acoustic Chern insulator [28], the Floquet lattices could be easily fabricated in a very large array for demonstrating functional topological devices such as a topological beam combiner and splitter (Supplemental Material Fig. S9 [38]), without the limitation of narrow operation bandwidth and other technical challenges, such as the ultrafast rotation speed of fan-like unit cells, the precise control of synchronous rotation of the spinning array, as well as the flow stability.

III. CONCLUSION

We propose a unique approach to implement chirality-assisted 3D Floquet lattices, which provides an acoustic analogue of electronic transport in Chern insulators by mapping the time dimension into the space dimension. The Floquet lattice can support broadband and low-loss cyclotron orbiting motion of chiral states both in the bulk and on the surface with reversed rotations. We show that the Weyl points are the phase transition points, at which the coupling strength $C = 0.25\pi$. In the strong coupling regime $C > 0.25\pi$, the topologically protected Fermi arc-like surface states are observed in the Floquet lattice. Splicing together two

Floquet lattices of reversed chiral structures, we demonstrate topological negative refraction with suppressed diffraction. For on-chip integration, we could resort to the mechanical counterpart with similar configurations, i.e., straight rods attached with chiral coupling channels, where the viscothermal loss can be ignored. Our simple and efficient design paves the way for versatile topological-insulator-based devices without incorporating pseudospin or valley degrees of freedom.

ACKNOWLEDGMENTS

This work was supported by the National Natural Science Foundation of China (Grants No. 11674119, No. 11774297, No. 11690030, and No. 11690032). J.Z. acknowledges the support from the Early Career Scheme (ECS) of Hong Kong RGC (Grant No. PolyU 252081/15E). X.F.Z. acknowledge the financial support from the Bird Nest Plan of HUST and Y.G.P. acknowledge the financial support from the China Scholarship Council (CSC).

---

[1] F. D. M. Haldane and S. Raghu, Phys. Rev. Lett. **100**, 013904 (2008).
[2] Z. Wang, Y. D. Chong, J. D. Joannopoulos, and M. Soljačić, Phys. Rev. Lett. **100**, 013905 (2008).
[3] Z. Wang, Y. D. Chong, J. D. Joannopoulos, and M. Soljačić, Nature (London) **461**, 772 (2009).
[4] M. Xiao, W. J. Chen, W. Y. He, and C. T. Chan, Nat. Phys. **11**, 920 (2015).
[5] R. Fleury, A. B. Khanikaev, and A. Alù, Nat. Commun. **7**, 11744 (2016).
[6] F. Li, X. Huang, J. Lu, J. Ma, and Z. Liu, Nat. Phys. **14**, 30 (2018).
[7] H. Ge, X. Ni, Y. Tian, S. K. Gupta, M. H. Lu, X. Lin, W. D. Huang, C. T. Chan, and Y. F. Chen, Phys. Rev. Appl. **10**, 014017 (2018).
[8] H. He, C. Qiu, L. Ye, X. Cai, X. Fan, M. Ke, F. Zhang, and Z. Liu, Nature (London) **560**, 61 (2018).
[9] C. He, X. Ni, H. Ge, X. C. Sun, Y. B. Chen, M. H. Lu, X. P. Liu, and Y. F. Chen, Nat. Phys. **12**, 1124 (2016).
[10] Z. G. Geng, Y. G. Peng, Y. X. Shen, D. G. Zhao, and X. F. Zhu, J. Phys. Condens.: Matter. **30**, 345401 (2018).
[11] Z. Zhang, Q. Wei, Y. Cheng, T. Zhang, D. Wu, and X. Liu, Phys. Rev. Lett. **118**, 084303 (2017).
[12] R. Chaunsali, C. W. Chen, and J. Yang, Phys. Rev. B **97**, 054307 (2018).
[13] S. Wu, Y. Wu, and J. Mei, New J. Phys. **20**, 023051 (2018).
[14] J. Lu, C. Qiu, M. Ke, and Z. Liu, Phys. Rev. Lett. **116**, 093901 (2016).
[15] J. Lu, C. Qiu, L. Ye, X. Fan, M. Ke, F. Zhang, and Z. Liu, Nat. Phys. **13**, 369 (2017).
[16] M. Wang, L. Ye, J. Christensen, and Z. Liu, Phys. Rev. Lett. **120**, 246601 (2018).
[17] Z. Zhang, Y. Tian, Y. Cheng, Q. Wei, X. Liu, and J. Christensen, Phys. Rev. Appl. **9**, 034032 (2018).
[18] Z. G. Geng, Y. G. Peng, Y. X. Shen, D. G. Zhao, and X. F. Zhu, Appl. Phys. Lett. **113**, 033503 (2018).
[19] Y. G. Peng, C. Z. Qin, D. G. Zhao, Y. X. Shen, X. Y. Xu, M. Bao, H. Jia, and X. F. Zhu, Nat. Commun. **7**, 13368 (2016).
[20] Y. G. Peng, Y. X. Shen, D. G. Zhao, and X. F. Zhu, Appl. Phys. Lett. **110**, 173505 (2017).
[21] Q. Wei, Y. Tian, S. Y. Zuo, Y. Cheng, and X. J. Liu, Phys. Rev. B **95**, 094305 (2017).
[22] For every energy eigenstate of a time-reversal symmetric system with half-integer spins, there exists one more eigenstate with the same energy. Kramers doublet is a featured characteristic in the Fermi or Fermi-like systems.
[23] A. Souslov, B. C. van Zuiden, D. Bartolo, and V. Vitelli, Nat. Phys. **13**, 1091 (2017).
[24] Z. G. Chen and Y. Wu, Phys. Rev. Appl. **5**, 054021 (2016).
[25] X. Ni, C. He, X. C. Sun, X. P. Liu, M. H. Lu, L. Feng, and Y. F. Chen, New J. Phys. **17**, 053016 (2015).
[26] A. B. Khanikaev, R. Fleury, S. H. Mousavi, and A. Alu, Nat. Commun. **6**, 8260 (2015).
[27] Z. Yang, F. Gao, X. Shi, X. Lin, Z. Gao, Y. Chong, and B. Zhang, Phys. Rev. Lett. **114**, 114301 (2015).
[28] Y. Ding, Y. Peng, Y. Zhu, X. Fan, J. Yang, B. Liang, X. Zhu, X. Wan, and J. Cheng, Phys. Rev. Lett. **122**, 014302 (2019).
[29] Q. Yan, R. Liu, Z. Yan, B. Liu, H. Chen, Z. Wang, and L. Lu, Nat. Phys. **14**, 461 (2018).
[30] Y. Yang, Z. Gao, H. Xue, L. Zhang, M. He, Z. Yang, R. Singh, Y. Chong, B. Zhang, and H. Chen, Nature (London) **565**, 622 (2019).
[31] B. Yang, Q. Guo, B. Tremain, R. Liu, L. E. Barr, Q. Yan, W. Gao, H. Liu, Y. Xiang, J. Chen, C. Fang, A. Hibbins, L. Lu, and S. Zhang, Science **359**, 1013 (2018).
[32] H. Jia, R. Zhang, W. Gao, Q. Guo, B. Yang, J. Hu, Y. Bi, Y. Xiang, C. Liu, and S. Zhang, Science **363**, 148 (2019).
[33] M. C. Rechtsman, J. M. Zeuner, Y. Plotnik, Y. Lumer, D. Podolsky, F. Dreisow, S. Nolte, M. Segev, and A. Szameit, Nature (London) **496**, 196 (2013).
[34] T. Kitagawa, E. Berg, M. Rudner, and E. Demler, Phys. Rev. B **82**, 235114 (2010).
[35] M. S. Rudner, N. H. Lindner, E. Berg, and M. Levin, Phys. Rev. X **3**, 031005 (2013).
[36] L. J. Maczewsky, J. M. Zeuner, S. Nolte, and A. Szameit, Nat. Commun. **8**, 13756 (2017).
[37] M. Z. Hasan and C. L. Kane, Rev. Mod. Phys. **82**, 3045 (2010).
[38] See Supplemental Material at http://link.aps.org/supplemental/10.1103/PhysRevResearch.1.033149 for the details on the sample design, the method of calculating projected band structures, and the experimental demonstration of topological transports induced by different boundary conditions in the Floquet lattices, which includes Refs. [34–36].
[39] Y. G. Peng, Z. G. Geng, and X. F. Zhu, J. Appl. Phys. **123**, 091716 (2018).
[40] R. Shankar, *Principles of Quantum Mechanics*, 2nd ed. (Springer Science+Business Media, Inc., 1994).
[41] Y. X. Shen, Y. G. Peng, D. G. Zhao, X. C. Chen, J. Zhu, and X. F. Zhu, Phys. Rev. Lett. **122**, 094501 (2019).